



Deterministic chaos in modulated multi-cell drifts of localized lower-hybrid oscillations excited by high-frequency waves in the ionosphere

Thomas B. Leyser

Swedish Institute of Space Physics, Uppsala, Sweden

Correspondence: Thomas B. Leyser (thomas.leyser@irfu.se)

Received: 9 October 2024 – Discussion started: 29 October 2024

Revised: 17 March 2025 – Accepted: 23 March 2025 – Published: 17 June 2025

Abstract. The prominent broad upshifted maximum (BUM) feature in electromagnetic emissions stimulated by powerful high-frequency radio waves in the ionosphere exhibits an exponential spectrum for pump frequencies near a harmonic of the ionospheric electron gyro frequency. Exponential power spectra are a characteristic of deterministic chaos. In the present treatment, a two-fluid model is derived for lower-hybrid (LH) oscillations driven by parametric interaction of the electromagnetic pump field, the electron Bernstein mode, and the upper-hybrid mode, as previously proposed to interpret the BUM. In two-dimensional geometry across the geomagnetic field, LH oscillations localized in cylindrical density depletions are associated with multi-cell plasma drift patterns. The numerical simulations show that topological modulations of the drift can give rise to approximately Lorentzian-shaped pulses in the LH time signal. For parameter values typical of the ionospheric experiments, the exponential power spectrum of the Lorentzian pulses has a slope that is consistent with the slope of the BUM spectrum. The BUM spectral structure is therefore attributed to deterministic chaos in LH dynamics.

1 Introduction

Electromagnetic emissions excited by powerful high-frequency (HF) electromagnetic waves transmitted into the ionosphere from the ground exhibit a rich spectral structure that depends notably on the pump frequency f_0 and its relation to a multiple s of the ionospheric electron gyro frequency f_e (Leyser, 2001). Figure 1 displays the most

prominent spectral feature of the stimulated electromagnetic emissions (SEEs), the so-called broad upshifted maximum (BUM), with its spectral maximum at $f_{\text{BUM}} \approx f_0 + 24$ kHz. The high-frequency flank of the BUM commonly exhibits an exponential power spectrum, with a constant slope in a semi-logarithmic plot. Also seen in Fig. 1 is a downshifted maximum (DM) at approximately $f_0 - 10$ kHz.

As first established in the fluid and nonlinear dynamics communities (Frisch and Morf, 1981; Greenside et al., 1982), exponential power spectra are a characteristic of deterministic chaos. Research on magnetically confined laboratory plasma showed that the associated time evolution consists of intermittent narrow pulses of Lorentzian shape (Pace et al., 2008) that arise because of topological modulations in the plasma drift trajectories in the vicinity of separatrices in the velocity field (Maggs and Morales, 2011, 2012). The topological modulations of a single-cell drift pattern can make pulses of plasma escape or enter the flow cell. In a multi-cell flow pattern, the modulations can make plasma pulses cross separatrices between the cells to switch the flow cell. Numerical simulations of structures formed by a temperature filament in magnetically confined plasma showed that Lorentzian pulses can arise due to the topological modulations of only two modes of coherent drift waves (Shi et al., 2009).

A Lorentzian pulse has the following functional form (Pace et al., 2008; Hornung et al., 2011; Maggs and Morales, 2011):

$$L(t) = \frac{A}{1 + \left(\frac{t-t_0}{\tau}\right)^2}, \quad (1)$$

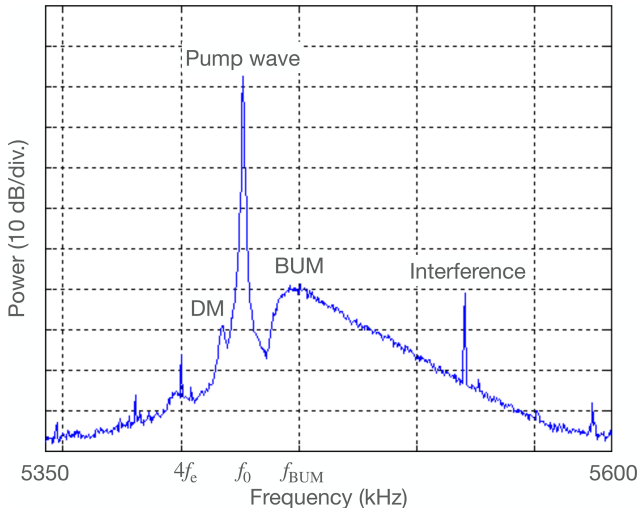


Figure 1. A BUM spectral feature observed in experiments at the SURA HF facility in Russia, with $f_0 = 5.426$ MHz, $4f_c \approx 5.407$ MHz, and $\Delta f_{BUM} \approx 24$ kHz (27 September 1998). Taken from Leyser (2021), where it is adapted from Carozzi et al. (2002).

where A is the amplitude of the pulse of width τ centred at time $t = t_0$. The Fourier transform of $L(t)$ is $\hat{L}(\omega) = A\tau\pi e^{i\omega t_0} e^{-\omega\tau}$, such that its power spectrum is

$$P(\omega) = A^2\tau^2\pi^2 \exp(-2\omega\tau). \tag{2}$$

A signal time series containing Lorentzian pulses of approximately equal widths τ will thus exhibit an exponential power spectrum $P(f) \propto \exp(-f/f_s)$ with a scaling frequency of $f_s = 1/(4\pi\tau)$.

A simplified model of the $\mathbf{E} \times \mathbf{B}_g$ drift associated with lower-hybrid (LH) oscillations localized in cylindrical geometry across the geomagnetic field \mathbf{B}_g (where \mathbf{E} is the electric field of the LH oscillations) suggested that deterministic chaos could also be excited by HF radio waves in the ionosphere (Leyser, 2021). It was shown that the drift trajectories can be chaotic in the localized multi-cell standing-wave pattern of the driving oscillations in the plane perpendicular to \mathbf{B}_g . This dynamic exhibits an exponential power spectrum that is consistent with that of the BUM feature in the SEE spectrum.

The frequency of the BUM f_{BUM} follows the empirical relation (Leyser et al., 1989; Leyser, 2001)

$$f_{BUM} - f_0 \approx f_0 - s f_c, \tag{3}$$

where $s \geq 3$. This dependence suggests that the BUM is excited by a parametric four-wave interaction. Huang and Kuo (1994) developed a one-dimensional analytical model involving an electromagnetic pump wave with an angular frequency and wave vector (ω_0, \mathbf{k}_0) , electron Bernstein (EB) waves $(\omega_1 \lesssim s\omega_e, \mathbf{k}_1)$, upper-hybrid (UH) waves $(\omega_2 = 2\pi f_{BUM} \gtrsim s\omega_e, \mathbf{k}_2)$, and non-resonant LH oscillations (ω_3, \mathbf{k}_3) . The matching conditions in their electrostatic

approximation are $\omega_1 + \omega_3 = \omega_0 = \omega_2 - \omega_3$ and $k_1 + k_3 = 0 = k_2 - k_3$. With this, $\omega_3 \ll \omega_1 \lesssim \omega_0 \lesssim \omega_2$ ($\omega_\alpha = 2\pi f_\alpha$ for $\alpha = 0, 1, 2, 3$). By assuming that the UH mode at $\omega_2 > \omega_0$ is converted to electromagnetic emissions by the scattering off of filamentary density striations, the emissions could propagate to the ground to be detected as the BUM in the SEE spectrum. The theoretical model was found to be consistent with experimental results and has been verified by numerical simulations of an electrostatic particle-in-cell model with one periodic space dimension and three velocity dimensions (Xi and Scales, 2001).

In the present treatment, a two-fluid model of LH oscillations excited by the beating of an electromagnetic pump field is presented, with EB and UH oscillations assumed to be localized in a cylindrical density depletion in the plane perpendicular to \mathbf{B}_g . This complements the study of parametric four-wave interactions by Huang and Kuo (1994) and focuses on the effects of an important nonlinear term for LH dynamics and considers two spatial dimensions. Further, the treatment expands on the study of Leyser (2021) by including the physics of LH oscillations instead of only the associated $\mathbf{E} \times \mathbf{B}_g$ drift. Simulation results are obtained with parameter values that are typical of those in electromagnetic pumping of ionospheric F-region plasma and show deterministic chaos in the LH dynamics and exponential power spectra that are consistent with what is observed for the BUM.

2 Theory

LH dynamics are described by a magnetized electron fluid and an unmagnetized ion fluid. For simplicity, the electron and ion fluids are taken here to be cold; i.e. the electron and ion temperatures are set to zero. All electric fields and velocities are considered to be in the x - y plane perpendicular to a static and homogeneous geomagnetic field $\mathbf{B}_g = B_g \hat{z}$.

The electron density is taken to be $n_e = n_s + n_3 + n_1 + n_2 \equiv n_s + n_3 + n_h$, where n_s is the static background electron density, and n_h contains the HF terms. The electron velocity is $\mathbf{v}_e = \mathbf{v}_0 + \mathbf{v}_1 + \mathbf{v}_2 + \mathbf{v}_3 \equiv \mathbf{v}_h + \mathbf{v}_3$, where \mathbf{v}_h contains the HF electron velocity terms. For reference, the quantities describing the four interacting wave modes are shown in Table 1. The force and charge continuity equations for \mathbf{v}_3 and n_3 at the LH timescale are as follows:

$$m_e \frac{\partial \mathbf{v}_3}{\partial t} = -e \mathbf{E}_3 - e \mathbf{v}_3 \times \mathbf{B}_g - m_e \langle (\mathbf{v}_h \cdot \nabla_\perp) \mathbf{v}_h \rangle - \nu_e m_e \mathbf{v}_3, \tag{4}$$

$$\frac{\partial n_3}{\partial t} + \nabla_\perp \cdot (n_e \mathbf{v}_e) = 0, \tag{5}$$

where $\nabla_\perp \equiv (\partial/\partial x)\hat{x} + (\partial/\partial y)\hat{y}$; \hat{x} and \hat{y} are unit vectors in the x and y directions, respectively; \mathbf{E}_3 is the LH electric field; and ν_e is the electron collision frequency (m_e and $-e$ are the electron mass and charge, respectively). The term $\mathbf{F} = m_e \langle (\mathbf{v}_h \cdot \nabla_\perp) \mathbf{v}_h \rangle$ is the ponderomotive force describing

the nonlinear low-frequency effect of the HF waves on the electrons, and the angular brackets denote an averaging of the enclosed quantities over the HF oscillations.

With the expressions for n_e and \mathbf{v}_e , Eq. (5) gives the following at the LH timescale:

$$\frac{\partial n_3}{\partial t} + (n_s + n_3)\nabla_{\perp} \cdot \mathbf{v}_3 + \mathbf{v}_3 \cdot \nabla_{\perp} n_3 = -\nabla_{\perp} \cdot \langle n_h \mathbf{v}_h \rangle. \quad (6)$$

The last (advection) term on the left-hand side is crucial to include the chaotic dynamics but has commonly been neglected in studies of nonlinear normal mode coupling of parametric interactions. For simplicity, this term is not included self consistently. To investigate the effect of the advection term, \mathbf{v}_3 is replaced by an externally provided drift velocity \mathbf{v}_D . Equation (6) is further simplified by $n_s \gg |n_3|$, neglecting the effect of static density inhomogeneity ($\nabla_{\perp} n_s = 0$) and taking $\nabla_{\perp} \cdot \langle n_h \mathbf{v}_h \rangle \approx 0$ (Istomin and Leyser, 1995), such that

$$\frac{\partial n_3}{\partial t} + n_s \nabla_{\perp} \cdot \mathbf{v}_3 + \mathbf{v}_D \cdot \nabla_{\perp} n_3 = 0. \quad (7)$$

By noting that the second term on the right-hand side of Eq. (4) is the largest, \mathbf{v}_3 can be obtained by iteration (Istomin and Leyser, 1995), giving

$$\begin{aligned} \mathbf{v}_3 = & \frac{e}{m_e \omega_e} \left(\frac{1}{B_g} \mathbf{E}_3 \times \mathbf{B}_g - \frac{1}{\omega_e} \frac{\partial \mathbf{E}_3}{\partial t} \right) \\ & - \frac{1}{m_e \omega_e} \left(\frac{1}{B_g} \mathbf{B}_g \times \mathbf{F} + \frac{1}{\omega_e} \frac{\partial \mathbf{F}}{\partial t} \right) \\ & - \frac{v_e}{\omega_e} \frac{1}{B_g} \mathbf{E}_3, \end{aligned} \quad (8)$$

where $\omega_e = 2\pi f_e = eB_g/m_e$, with the last term being included to account for collisional damping. The ponderomotive force is taken to be (Istomin and Leyser, 1995)

$$\mathbf{F} = \frac{1}{8} \frac{e^2}{m_e (\omega_0 + \omega_e)^2} \nabla_{\perp} |E_h|^2. \quad (9)$$

$\mathbf{E}_h = \mathbf{E}_0 + \mathbf{E}_1 + \mathbf{E}_2$ is the total HF electric field. For simplicity, an additional term that depends on the electron gyroharmonic s derived by Istomin and Leyser (1995) has been neglected.

Substituting Eq. (8) into Eq. (7) to eliminate \mathbf{v}_3 gives

$$\frac{\partial n_3}{\partial t} = \frac{en_s}{m_e \omega_e^2} \left(\frac{\partial}{\partial t} + v_e \right) \nabla_{\perp} \cdot \mathbf{E}_3 + \frac{n_s}{m_e \omega_e^2} \frac{\partial}{\partial t} (\nabla_{\perp} \cdot \mathbf{F}). \quad (10)$$

With the Poisson equation $\varepsilon_0 \nabla_{\perp} \cdot \mathbf{E}_3 = e(n_{i3} - n_3)$, an equation relating the electron density fluctuations n_3 to those of the ion density n_{i3} is obtained as follows (ε_0 is the vacuum permittivity):

$$\begin{aligned} \frac{\partial n_3}{\partial t} = & \frac{\omega_p^2}{\omega_{uh}^2} \frac{\partial n_{i3}}{\partial t} + v_e \frac{\omega_p^2}{\omega_{uh}^2} (n_{i3} - n_3) - \frac{\omega_e^2}{\omega_{uh}^2} \mathbf{v}_D \cdot \nabla_{\perp} n_3 \\ & + \frac{n_s}{m_e \omega_{uh}^2} \frac{\partial}{\partial t} (\nabla_{\perp} \cdot \mathbf{F}), \end{aligned} \quad (11)$$

where $\omega_{uh}^2 = \omega_p^2 + \omega_e^2$, and ω_p is the electron plasma frequency.

The force and charge continuity equations for the unmagnetized ion fluid are, similarly,

$$m_i \frac{\partial \mathbf{v}_{i3}}{\partial t} = e \mathbf{E}_3 - \nu_i m_i \mathbf{v}_{i3}, \quad (12)$$

$$\frac{\partial n_{i3}}{\partial t} + (n_s + n_{i3}) \nabla_{\perp} \cdot \mathbf{v}_{i3} + \mathbf{v}_D \cdot \nabla_{\perp} n_{i3} = 0, \quad (13)$$

where ν_i is the ion collision frequency. Eliminating \mathbf{v}_{i3} and using, again, the Poisson equation to eliminate \mathbf{E}_3 results in

$$\begin{aligned} \left(\frac{\partial^2}{\partial t^2} + \omega_{pi}^2 + \nu_i \frac{\partial}{\partial t} \right) n_{i3} = & \omega_{pi}^2 n_3 - \frac{\partial \mathbf{v}_D}{\partial t} \cdot \nabla_{\perp} n_{i3} \\ & - \mathbf{v}_D \cdot \nabla_{\perp} \frac{\partial n_{i3}}{\partial t}. \end{aligned} \quad (14)$$

Equations (11) and (14) are a coupled set of equations for the electron and ion densities, with n_3 and n_{i3} being associated with the LH dynamics driven by the external fields through \mathbf{F} and \mathbf{v}_D .

In order to relate the electromagnetic pump and EB, UH, and LH fields to one another through \mathbf{F} and \mathbf{v}_D , it is recalled that the empirical relation in Eq. (3) suggests that the BUM is excited by a parametric four-wave interaction. In two-dimensional cylindrical geometry, the matching conditions are (Karplyuk et al., 1970; Leyser, 2021)

$$\omega_1 + \omega_3 = \omega_0 = \omega_2 - \omega_3, \quad (15)$$

$$m_1 + m_3 = m_0 = m_2 - m_3, \quad (16)$$

where m_{α} is the azimuthal mode number ($\alpha = 0, 1, 2, 3$). In cylindrical geometry, there are no matching conditions for the radial wave numbers $k_{r\alpha}$.

The ponderomotive force \mathbf{F} depends on the HF fields \mathbf{E}_h . With the electric fields having the time dependence $\mathbf{E}_{\alpha} \propto \cos(\omega_{\alpha} t)$, the following terms in relation to \mathbf{F} include components that can excite LH oscillations at ω_3 according to the matching condition of Eq. (15):

$$|E_h|^2 = \mathbf{E}_0 \cdot \mathbf{E}_1 + \mathbf{E}_0 \cdot \mathbf{E}_2. \quad (17)$$

The pump field is taken to be left-handedly circularly polarized (for which the electric field rotates in opposition to the electron gyro motion):

$$\mathbf{E}_0 = \frac{E_0}{\sqrt{2}} [\cos(\omega_0 t) \hat{x} - \sin(\omega_0 t) \hat{y}]. \quad (18)$$

The EB ($\alpha = 1$) and UH ($\alpha = 2$) oscillations are taken to have the potential

$$\Phi_{\alpha} = A_{\alpha} J_{m_{\alpha}}(k_{r\alpha} \rho) \cos(m_{\alpha} \varphi + \Delta \varphi_{\alpha}) \cos(\omega_{\alpha} t), \quad (19)$$

such that $\mathbf{E}_{\alpha} = -\nabla_{\perp} \Phi_{\alpha}$, where $J_{m_{\alpha}}$ is the Bessel function of the first kind, $\rho = (x^2 + y^2)^{1/2}$, φ is the azimuthal angle in

Table 1. Parameters for the four wave modes responsible for the broad upshifted maximum (BUM).

Mode	Density	Velocity	Frequency	Conditions
Ambient	n_s	$\mathbf{v}_s = \mathbf{0}$	$f_s = 0$	Stationary
Electromagnetic	n_0	\mathbf{v}_0	f_0	Pump wave
Electron Bernstein (EB)	n_1	\mathbf{v}_1	f_1	$f_1 \lesssim s f_e$
Upper hybrid (UH)	n_2	\mathbf{v}_2	f_2	$f_2 = f_{\text{BUM}} \gtrsim s f_e$
Lower hybrid (LH)	n_3	\mathbf{v}_3	f_3	$f_3 \approx f_0 - f_1 \approx f_2 - f_0$
High frequency (HF)	n_h	\mathbf{v}_h	f_0	$n_h = n_0 + n_1 + n_2, \mathbf{v}_h = \mathbf{v}_0 + \mathbf{v}_1 + \mathbf{v}_2$

the x - y plane, and $\Delta\varphi_\alpha$ accounts for a possible phase shift between the EB and UH oscillations. With Eqs. (18) and (19) being incorporated into Eq. (17), an expression for \mathbf{F} , as in Eq. (9), is obtained.

The largest contribution to \mathbf{v}_3 in Eq. (8) is the first term on the right-hand side, which is proportional to $\mathbf{E}_3 \times \mathbf{B}_g$. The drift velocity \mathbf{v}_D , which has to be provided, is therefore taken to be $\mathbf{v}_D = \mathbf{E}_D \times \mathbf{B}_g / B_g$, where \mathbf{E}_D is associated with the beating of the HF fields that give contributions at ω_3 . For the present purpose, $\mathbf{E}_D = -\nabla_\perp \Phi_D$:

$$\Phi_D = [A_{01} J_{m_3}(k_{r1}\rho) \cos(m_3\varphi) + A_{02} J_{m_3}(k_{r2}\rho) \times \cos(m_3\varphi + \Delta\varphi_2)] \cos(\omega_3 t) e^{-\rho/L}, \tag{20}$$

where A_{01} (A_{02}) is the potential that results from the beating at ω_3 of the pump field and EB (UH) oscillations and is therefore proportional to the product of E_0 and the amplitude A_1 (A_2) of the EB (UH) oscillations; see Eq. (19). However, it is beyond the scope of the present treatment to derive a relation between them. The focus here is to study the possible influence of the externally provided \mathbf{F} and \mathbf{v}_D on LH dynamics. The last factor in Eq. (20) is used to model the localization of Φ_D in relation to LH oscillations in a cylindrical density depletion, where L is the decay scale length of the potential outside of the depletion.

3 Simulation scheme

Solutions to Eqs. (11) and (14) are computed numerically. Hereafter, the dimensionless density variables $\eta_3 \equiv n_3(t, x, y) / n_s$ and $\eta_{i3} \equiv n_{i3} / n_s$ will be used. Further, Eq. (14) is of the second order in the time derivative. In order to solve it numerically, it is converted into two first-order equations by introducing $\eta'_{i3} \equiv n'_{i3} / n_s$. This gives the following set of three equations:

$$\frac{\partial \eta_3}{\partial t} = \frac{\omega_p^2}{\omega_{\text{uh}}^2} \eta'_{i3} + (\eta_{i3} - \eta_3) v_e - \frac{\omega_e^2}{\omega_{\text{uh}}^2} \mathbf{v}_D \cdot \nabla_\perp \eta_3 + \frac{1}{m_e \omega_{\text{uh}}^2} \frac{\partial}{\partial t} (\nabla_\perp \cdot \mathbf{F}), \tag{21}$$

$$\frac{\partial \eta'_{i3}}{\partial t} = \omega_{\text{pi}}^2 (\eta_3 - \eta_{i3}) - v_i \eta'_{i3} - \frac{\partial \mathbf{v}_D}{\partial t} \cdot \nabla_\perp \eta_{i3} - \mathbf{v}_D \cdot \nabla_\perp \eta'_{i3}, \tag{22}$$

$$\frac{\partial \eta_{i3}}{\partial t} = \eta'_{i3}. \tag{23}$$

To solve Eqs. (21) to (23) numerically, they are converted into a system of coupled algebraic equations by replacing η_3 , η_{i3} , and η'_{i3} with corresponding grid functions that are discretized in time $t = t_j = j \Delta t$ ($j = 0, 1, 2, \dots, J$) and on an equidistant spatial grid of $x = x_k = k \Delta d$ and $y = y_l = l \Delta d$ ($k, l = 0, 1, 2, \dots, M$), such that $\eta_3(t_j, x_k, y_l) \approx \eta_3^{jkl}$, $\eta_{i3}(t_j, x_k, y_l) \approx \eta_{i3}^{jkl}$, and $\eta'_{i3}(t_j, x_k, y_l) \approx \eta_{i3'}^{jkl}$ (Langtangen and Linge, 2017).

The time derivatives of η_3 , η_{i3} , and η'_{i3} are approximated with the forward Euler method for the finite differences; for example, $\partial \eta_3 / \partial t \approx (\eta_3^{(j+1)kl} - \eta_3^{jkl}) / \Delta t$. All spatial differences are computed at the time step j . Second-order spatial derivatives are approximated by centred differencing; for example, $\partial^2 E_{\alpha x} / \partial x^2 \approx (E_{\alpha x}^{j(k+1)l} - 2E_{\alpha x}^{jkl} + E_{\alpha x}^{j(k-1)l}) / \Delta x^2$. The first-order spatial derivatives of η_3 , η_{i3} , and η'_{i3} in the advection terms need a different treatment and are approximated by so-called upwind differencing. For example, in the x direction, with η_3 , we take $\partial \eta_3 / \partial x \approx (\eta_3^{jkl} - \eta_3^{j(k-1)l}) / \Delta x$ when $v_{Dx} > 0$ and $\partial \eta_3 / \partial x \approx (\eta_3^{j(k+1)l} - \eta_3^{jkl}) / \Delta x$ when $v_{Dx} < 0$. The direction of the differencing is always against the direction of the drift.

The spatial grid is 4.0×4.0 m, with $\Delta d \approx 0.025$ m. The fields are localized around the centre of the grid $(x, y) = (0, 0)$ m by multiplication of a factor $\exp(-\rho/L)$ with $L = 0.4$ m. All parameters are zero at the boundaries: $\eta_3^{j0l} = \eta_3^{jMl} = 0$ and $\eta_3^{jk0} = \eta_3^{jkM} = 0$, $\eta_{i3}^{j0l} = \eta_{i3}^{jMl} = 0$ and $\eta_{i3}^{jk0} = \eta_{i3}^{jkM} = 0$, and $\eta_{i3'}^{j0l} = \eta_{i3'}^{jMl} = 0$ and $\eta_{i3'}^{jk0} = \eta_{i3'}^{jkM} = 0$.

The time step is $\Delta t = 2.5 \times 10^{-7}$ s. The initial conditions of the spatial grid are taken such that $\eta_3^{0kl} \propto \Phi_D(t = 0)$ in Eq. (20):

$$\eta_3^{0kl} = \frac{N_3}{(A_{01}^2 + A_{02}^2)^{1/2}} (A_{01} J_{m_1}(k_{r1}\rho_{kl}) \cos(m_1\varphi_{kl}) + A_{02} J_{m_2}(k_{r2}\rho_{kl}) \cos(m_2\varphi_{kl} + \Delta\varphi_2)) e^{-\rho/L}, \tag{24}$$

where A_{01} and A_{02} allow for different relative amplitudes of the EB and UH potentials. Further, $\eta_{i3}^{0kl} = (\omega_{\text{uh}}^2 / \omega_p^2) \eta_3^{0kl}$, and $\eta_{i3'}^{0kl} = 0$.

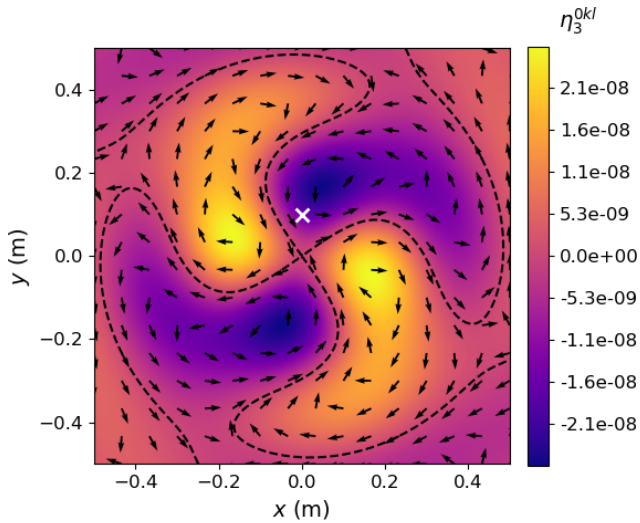


Figure 2. Initial relative electron density distribution η_3^{0kl} for the LH oscillations in the centre of the 4×4 m simulation plane according to Eq. (24) ($N_3 = 1.0 \times 10^{-7}$, $A_{01} = A_{02} = 0.2$ V, $\Delta\varphi_2 = \pi/2$). The arrows indicate the direction of the $\mathbf{E}_D \times \mathbf{B}_g$ drift. The dashed lines delineate $\eta_3^{0kl} = 0$, constituting separatrices for the drift. The white cross at $(x, y) = (0.0, 0.1)$ m marks the position where the time signal and power spectrum are shown in the subsequent figures. The position is relatively near an initial separatrix of the drift.

4 Simulation results

As an example, the azimuthal mode numbers of the interacting wave modes are taken to be $m_0 = 1$, $m_1 = -1$, and $m_2 = 3$, which, using Eq. (16), gives $m_3 = 2$. In the experiments, the transmitted electromagnetic pump wave is approximately a left-handed circularly polarized plane wave on the small-spatial-scale lengths of interest here, propagating nearly parallel to \mathbf{B}_g . However, its scattering on filamentary density depletions with much-smaller-spatial-scale lengths transverse to \mathbf{B}_g compared to the electromagnetic wavelength can give an azimuthal component of the pump field (Istomin and Leyser, 2003). This is the motivation for why $m_0 = 1$ is taken here, which implies that $m_1 \neq m_2$ for $m_3 \neq 0$. Figure 2 shows the initial η_3^{0kl} , as given by Eq. (24), in the centre of the simulation plane perpendicular to \mathbf{B}_g . The magnitude of $N_3 = 1.0 \times 10^{-7}$ is chosen, such that \mathbf{F} in the right-hand side of Eq. (21) has an effect on the temporal evolution, with reasonable values for the external amplitudes E_0 , A_1 , A_2 , A_{01} , and A_{02} .

Figure 3 displays the computed electron and ion densities – η_3^{jkl} (blue) and η_{i3}^{jkl} (red), respectively – at $(x, y) = (0.0, 0.1)$ m for (a) $E_0 = 0.001$ V m $^{-1}$ and $A_{01} = A_{02} = 0.002$ V and (b) $E_0 = 0.1$ V m $^{-1}$ and $A_{01} = A_{02} = 0.2$ V, with $A_1 = A_2 = 0.2$ V in both cases. Parameters typical of the ionospheric F region were used: $\omega_e \approx 2\pi \times 1.35 \times 10^6$ s $^{-1}$, as estimated from the experiments (Carozzi et al., 2002) from which the spectrum in Fig. 1 was obtained, oxy-

gen ions; $\omega_{uh} = s \omega_e$, with $s = 4$, $v_e = 500$ s $^{-1}$, and $v_i = 5$ s $^{-1}$; and electron temperature $T_e = 2000$ K. The frequencies of the involved wave modes are related by the matching condition of Eq. (15), where, for the present treatment, $\omega_1 = 4\omega_e - \Delta\omega_1$, where $\Delta\omega_1 = 2\pi \times 10 \times 10^3$ s $^{-1}$. By keeping ω_1 constant, k_{r1} is constant, while, for the small value of $\Delta\omega_1$, we still have $\omega_0 \approx 4\omega_e$ for the different ω_3 values to be discussed. In the experiments, $\omega_0 \approx 4\omega_e$ commonly results in the exponential slope of the BUM spectral feature that is of interest here.

In Fig. 3a, the external driving due to E_0 is weak, such that \mathbf{v}_D and \mathbf{F} in Eqs. (21) and (22) are small. The displayed oscillations are the LH resonance oscillations at about 7.6 kHz that are weakly perturbed by the beating of the HF fields at $f_3 = 20$ kHz in \mathbf{v}_D and \mathbf{F} . For comparison, a sinusoidal oscillation at f_3 is shown in black. The oscillation frequency in Fig. 3a agrees with the theoretical value of the LH resonance frequency:

$$f_{lh} = \frac{1}{2\pi} \frac{\omega_{pi}\omega_e}{\omega_{uh}} = \left(\frac{m_e}{m_i}\right)^{1/2} \left(1 - \frac{1}{s^2}\right)^{1/2} f_e \approx 7.6 \text{ kHz}, \quad (25)$$

where $\omega_{pi} = (m_e/m_i)^{1/2}\omega_p$. The time step in the computations – $\Delta t = 2.5 \times 10^{-7}$ s – implies $\Delta t f_{lh} \approx 1.9 \times 10^{-3}$. In Fig. 3b, E_0 is sufficiently strong, such that the temporal evolution is instead determined by \mathbf{v}_D and \mathbf{F} . The temporal evolution contains narrow pulses that are even shorter than the oscillations at the driving frequency f_3 illustrated in Fig. 3a.

Figure 4 displays the temporal evolution (panel a) of η_3^{jkl} (blue) and η_{i3}^{jkl} (red) and the corresponding power spectrum (panel b) for the longer time period from $t = 0$ s to $t = 0.0025$ s, with the same parameter values as for Fig. 3b. The power spectrum is approximately exponential as it has a constant slope in the semi-logarithmic plot. The narrow peaks at multiples of $f_3 = 20$ kHz enter through \mathbf{v}_D and \mathbf{F} in Eqs. (21) and (22). The width of the LH spectrum is about 160 kHz, which is an order of magnitude larger than both f_{lh} and f_3 .

In Figs. 5 and 6, some of the narrow pulses in the temporal evolution of η_3^{jkl} in Fig. 4a are investigated. Figure 5a shows η_3^{jkl} from $t = 0.0005$ s to $t = 0.0025$ s, which corresponds to a timescale of $0.0005 \times f_{lh} \approx 4$ to $0.0025 \times f_{lh} \approx 19$ wave periods of LH resonance oscillations. The time period excludes the initial overshoot behaviour of η_3^{jkl} seen in Fig. 4a. The four pairs of vertical dashed red lines mark the time periods with pulse-type features discussed in Fig. 5b and c ($t \approx 0.00067$ s) and Fig. 6 ($t \approx 0.00092$, 0.00182 , and 0.00214 s). Figure 5b displays an expanded time period marked by the vertical dashed red lines at $t \approx 0.00067$ s, which includes a single negative pulse-type feature in the time series (blue dots) together with a fitted Lorentzian function in accordance with Eq. (1) (black curve). The width of the Lorentzian pulse is $\tau \approx 8.90 \times 10^{-6}$ s, such that $\tau f_3 \approx 0.18$, which implies that the temporal pulse is much shorter than the driving wave period ($1/f_3$). The corresponding scal-

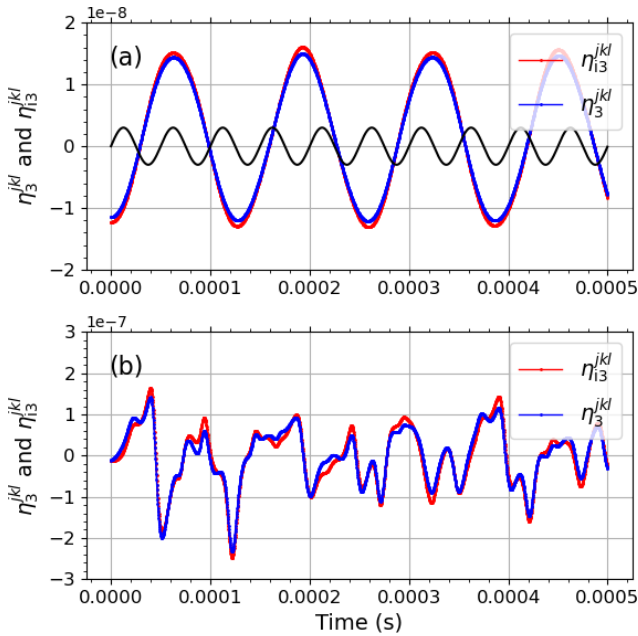


Figure 3. Temporal evolution of η_3^{jkl} and η_{i3}^{jkl} at k and l , such that $(x, y) = (0.0, 0.1)$ m from 0 to 0.0005 s ($f_3 = 20$ kHz, $\Delta\varphi_2 = \pi/2$). (a) $E_0 = 0.001$ V m $^{-1}$, $A_1 = A_2 = 0.2$ V, and $A_{01} = A_{02} = 0.002$ V. For comparison, shown in black is an oscillation $\sin(\omega_3 t)$ at the driving frequency f_3 . (b) $E_0 = 0.1$ V m $^{-1}$, $A_{01} = A_{02} = 0.2$ V, and other parameter values as for (a).

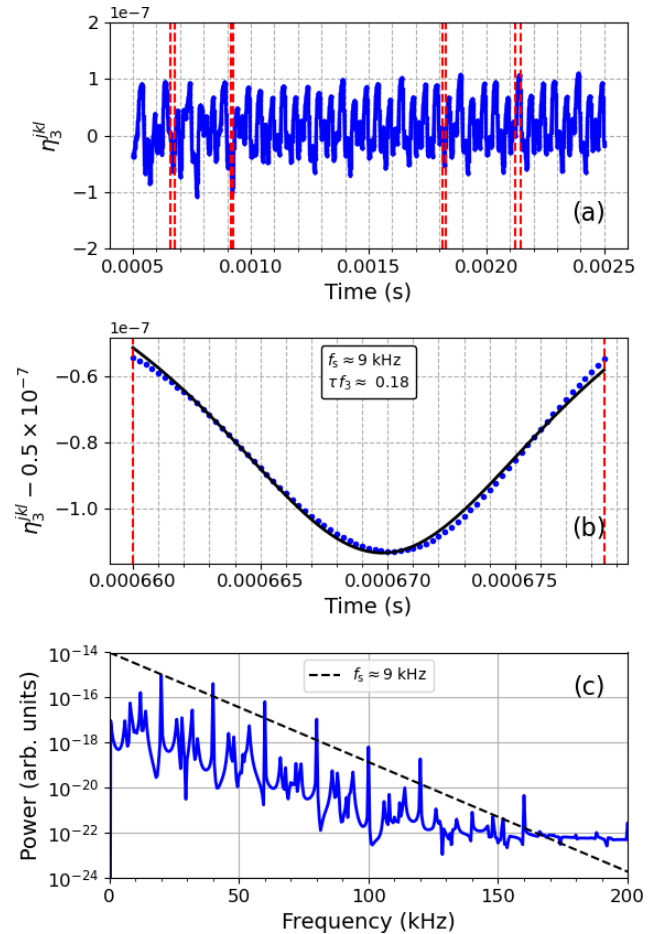


Figure 5. Fit of a Lorentzian function to a single pulse-type feature in the signal of η_3^{jkl} for the same time series as in Fig. 4 ($f_3 = 20$ kHz and $E_0 = 0.1$ V m $^{-1}$). (a) Temporal evolution from $t = 0.0005$ s to $t = 0.0025$ s and (b) for a single pulse (blue dots). The time period for the single pulse is marked by the leftmost pair of vertical dashed red lines at $t \approx 0.0067$ s in (a). The three remaining pairs of vertical dashed lines indicate the time periods discussed in Fig. 6. The solid black curve in (b) is a fitted Lorentzian pulse of width $\tau \approx 8.90 \times 10^{-6}$ s, which corresponds to $f_s \approx 9$ kHz. (c) The power spectrum for the time series in (a). The dashed line shows the exponential slope $P = 10^{-6} \exp(-f/f_s)$.

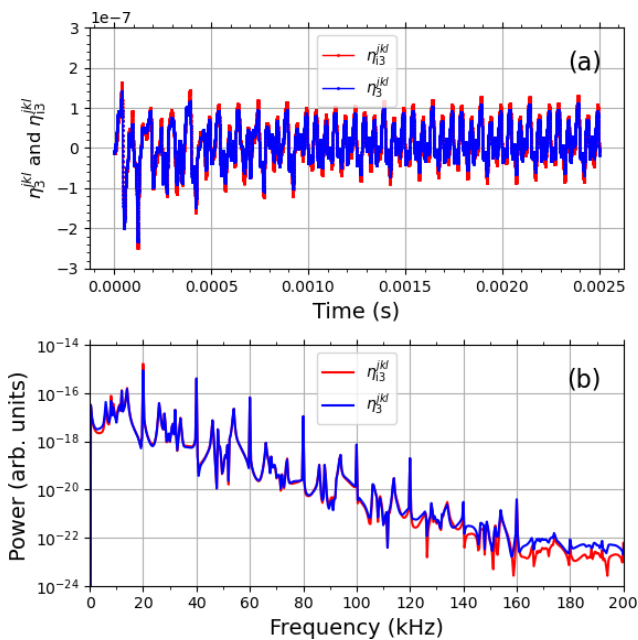


Figure 4. Temporal evolution (a) and power spectrum (b) of η_3^{jkl} (blue) and η_{i3}^{jkl} (red) at $(x, y) = (0.0, 0.1)$ m for the time between 0 s and 0.0025 s, with the same parameter values as for Fig. 3b.

ing frequency is $f_s = 1/(4\pi\tau) \approx 9$ kHz. Figure 5c shows the power spectrum (blue) of the time series in Fig. 5a, together with $P(f) \propto \exp(-f/f_s)$ (dashed black line). The width τ and corresponding scaling frequency f_s of the approximately Lorentzian-shaped pulse in Fig. 5b correspond roughly to the slope of the spectrum.

Figure 6 displays three additional pulse-type features in the same time series of η_3^{jkl} (Figs. 4 and 5a) from the time periods at (a) $t \approx 0.00092$ s, (b) $t \approx 0.00182$ s, and (c) $t \approx 0.00214$ s, marked by the three rightmost pairs of dashed red vertical lines in Fig. 5a. In Fig. 6a, the fitted Lorentzian pulse has a width of $\tau \approx 6.15 \times 10^{-6}$ s and $f_s \approx 13$ kHz. In

Fig. 6b, the fitted Lorentzian pulse is $\tau \approx 7.23 \times 10^{-6}$ s and $f_s \approx 11$ kHz. Most of the pulse-type features in the time series in Fig. 5a have a skewed shape, and only a few have a reasonably symmetric Lorentzian form. Figure 6c shows an example of a skewed pulse. A Lorentzian function cannot be reasonably fitted to the pulse. In Fig. 6d, the same spectrum as in Fig. 5c is displayed but with the spectral slopes for the obtained f_s of the Lorentzian functions: (a) $f_s \approx 13$ kHz (dotted line) and (b) $f_s \approx 11$ kHz (dash-dotted line). The Lorentzian pulse widths are consistent with the slope of the spectrum. As different widths of Lorentzian pulses give different f_s values, an observed exponential predominantly Lorentzian pulses of approximately equal width, as for Fig. 5b ($f_s \approx 9$ kHz), Fig. 6a ($f_s \approx 13$ kHz), and Fig. 6b ($f_s \approx 11$ kHz).

The width τ of the approximately Lorentzian-shaped pulses in the time series η_3^{jkl} at a given (x, y) depends on the amplitudes $E_0, A_1, A_2, A_{01},$ and A_{02} . Figure 7 displays a case with $E_0 = 0.2 \text{ V m}^{-1}, A_{01} = A_{02} = 0.4 \text{ V},$ and other parameters, as for Figs. 4 to 6, for which $E_0 = 0.1 \text{ V m}^{-1}$ and $A_{01} = A_{02} = 0.2 \text{ V}$. Figure 7a shows the time series at $(x, y) = (0.0, 0.1) \text{ m}$. The two pairs of dashed red lines at $t \approx 0.00057 \text{ s}$ and $t \approx 0.00077 \text{ s}$ indicate two examples of negative pulse-type signatures that have approximately Lorentzian shapes. In Fig. 7b, the pulse (blue dots) at $t \approx 0.00057 \text{ s}$ is displayed together with a fitted Lorentzian function (black line) with a width corresponding to $f_s \approx 13$ kHz. In Fig. 7c, the pulse (blue dots) at $t \approx 0.00077 \text{ s}$ is shown with a fitted Lorentzian function (black line) with a width corresponding to $f_s \approx 15$ kHz. The associated exponential slopes agree approximately with that of the power spectrum of the time series seen in Fig. 7d. The pulse in Fig. 7c with $f_s \approx 15$ kHz appears to have a slightly better fit to the spectrum. The obtained scaling frequencies of $f_s \approx 13$ kHz and $f_s \approx 15$ kHz are a few kilohertz higher than those in Figs. 5 and 6, for which $f_s \approx 9, 11,$ and 13 kHz. Stronger driving through $E_0, A_{01},$ and A_{02} gives a larger drift $-v_D = E_D \times B_g/B_g -$ and, thereby, narrower pulses with larger f_s .

5 Discussion

Plasma drifts in multi-cell patterns may exhibit deterministic chaos due to topological modulations of the flow (e.g. Shi et al., 2009; Maggs and Morales, 2011, 2012). The topological modulations result in the formation of narrow temporal pulses of Lorentzian shape in the plasma flow. As the power spectrum of a Lorentzian pulse is exponential, it follows that, if the Lorentzian pulses in the time signal have approximately the same widths, its spectrum will be exponential. Exponential power spectra are an inherent characteristic of deterministic chaos.

The BUM feature in the spectrum of electromagnetic emissions stimulated by powerful radio waves in the iono-

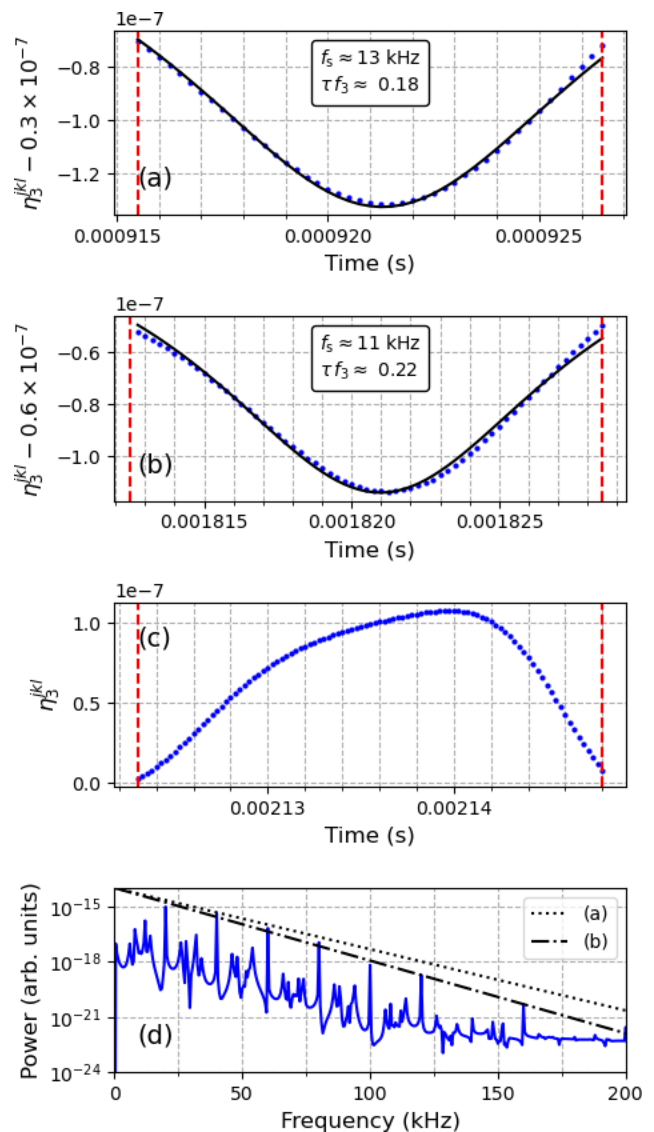


Figure 6. Three examples of pulse-type features from the computed time series η_3^{jkl} (blue dots) in Figs. 4 and 5a and fits of a Lorentzian function (black lines). (a) Pulse at $t \approx 0.00092$ s and fitted Lorentzian function with $f_s \approx 13$ kHz (η_3^{jkl} was decreased by 0.3×10^{-7} to optimize the fit). (b) Pulse at $t \approx 0.00182$ s and $f_s \approx 11$ kHz (η_3^{jkl} was decreased by 0.6×10^{-7} to optimize the fit). (c) Pulse at $t \approx 0.00214$ s. (d) The power spectrum (the same as in Fig. 5c), with the black lines showing the exponential slope $P = 10^{-14} \exp(-f/f_s)$ for the pulses in (a) and (b).

sphere commonly exhibits an exponential high-frequency flank, as shown in Fig. 1. The BUM has been attributed to parametric four-wave interactions involving the electromagnetic pump wave and electrostatic EB, UH, and LH waves (Huang and Kuo, 1994), with matching conditions for the high-frequency waves, as suggested by the empirical relation in Eq. (3). In the theory, the UH oscillations at $\omega_2 = \omega_0 + \omega_3$ are assumed to scatter off small-scale density irregularities

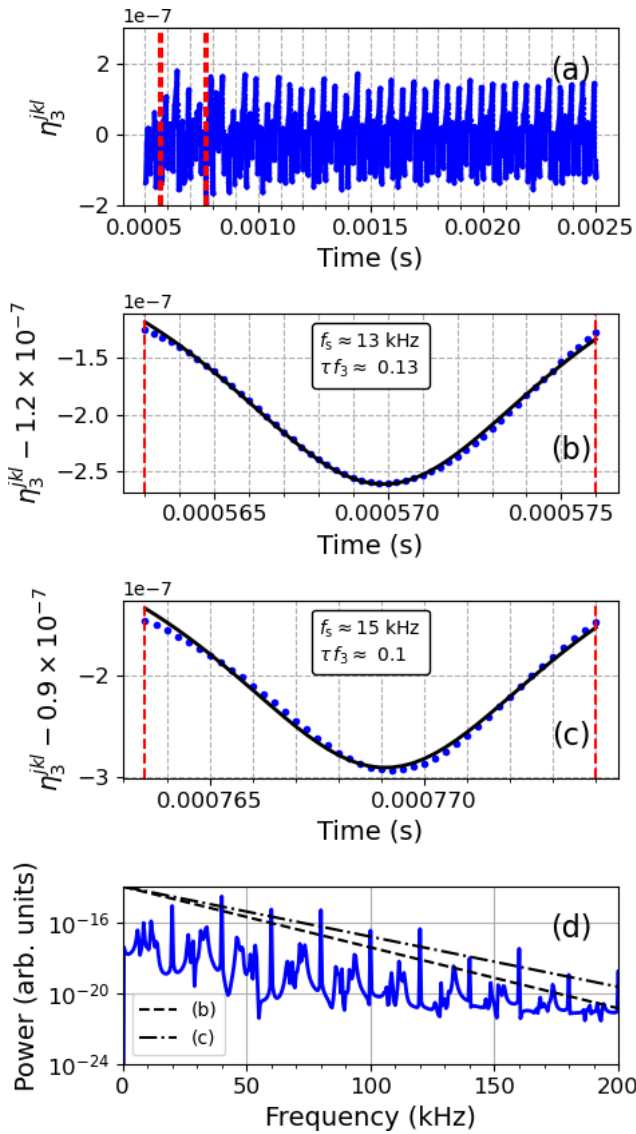


Figure 7. Lorentzian pulse-type features in the computed time signal of η_3^{jkl} at $(x, y) = (0.0, 0.1)$ m for $E_0 = 0.2 \text{ V m}^{-1}$, $A_{01} = A_{02} = 0.4 \text{ V}$, and other parameter values, as for Figs. 4 to 6. (a) Temporal evolution from $t = 0.0005 \text{ s}$ to $t = 0.0025 \text{ s}$. Two pulses are indicated by the two pairs of vertical red dashed lines. (b) Pulse (blue dots) at $t \approx 0.00057 \text{ s}$ and fitted Lorentzian function (solid black curve) of width $\tau \approx 6.27 \times 10^{-6} \text{ s}$, which corresponds to $f_s \approx 13 \text{ kHz}$ (η_3^{jkl} was decreased by 1.2×10^{-7} to optimize the fit). (c) Pulse (blue dots) at $t \approx 0.00077 \text{ s}$ and fitted Lorentzian function (solid black curve) of width $\tau \approx 5.25 \times 10^{-6} \text{ s}$, which corresponds to $f_s \approx 15 \text{ kHz}$ (η_3^{jkl} was decreased by 0.9×10^{-7} to optimize the fit). (d) The power spectrum for the time series in (a). The black lines show the exponential slope $P = 10^{-14} \exp(-f/f_s)$ for f_s in (b) and (c).

into electromagnetic emissions that can escape the ionosphere and be detected as the BUM on the ground. Whereas the initial theory by Huang and Kuo (1994) considered waves in one spatial dimension, the present understanding is that, on thermal timescales, wave modes perpendicular to \mathbf{B}_g are localized inside density depletions of small-scale striations (Gurevich et al., 1997; Mjølhus, 1997; Istomin and Leyser, 1998). In two-dimensional geometry perpendicular to \mathbf{B}_g , excited localized wave modes will have standing multi-cell oscillations inside the density depletions.

In the present treatment, results of numerical simulations of relevant nonlinear wave processes are presented. LH oscillations are modelled by Eqs. (11) and (14) in the plane perpendicular to \mathbf{B}_g and are excited by nonlinear interactions of the pump and EB and UH modes. Specifically, the beating of the pump field with the EB and UH fields is introduced through the ponderomotive force \mathbf{F} and the drift velocity \mathbf{v}_D in the advection terms in the equations. Figure 2 shows the initial condition for the electron density fluctuations η_3^{0kl} . With $\eta_3^{0kl} \propto \Phi_D(t=0)$, the $\mathbf{E}_D \times \mathbf{B}_g$ drift occurs along equipotential lines around extrema in η_3^{jkl} . Thus, the direction of the $\mathbf{E}_D \times \mathbf{B}_g$ drift changes from clockwise to anti-clockwise and vice versa in adjacent extrema in Φ_D and η_3^{jkl} . The resulting separatrices in the $\mathbf{E}_D \times \mathbf{B}_g$ drift are illustrated by dashed lines in Fig. 2. Also, the drift changes direction with the change in sign of \mathbf{E}_D every half wave period $T_3/2 = 1/(2f_3)$.

Figure 3 displays the temporal evolution of the LH electron η_3^{jkl} (blue) and ion η_{i3}^{jkl} (red) density fluctuations at $(x, y) = (0.0, 0.1)$ m for (a) $E_0 = 0.001 \text{ V m}^{-1}$ and $A_{01} = A_{02} = 0.002 \text{ V}$ and (b) $E_0 = 0.1 \text{ V m}^{-1}$ and $A_{01} = A_{02} = 0.2 \text{ V}$, with $f_3 = 20 \text{ kHz}$ and $A_1 = A_2 = 0.2 \text{ V}$ in both cases. In Fig. 3a, η_3^{jkl} and η_{i3}^{jkl} oscillate at the LH resonance frequency of 7.6 kHz , which is lower than at f_3 . Because of the low E_0 , the external driving through \mathbf{F} and \mathbf{v}_D at f_3 is too weak to have a noticeable effect on the time dependence. However, in Fig. 3b, the temporal evolution is different, with pulse-type features occurring seemingly erratically, some of which are narrower than the driving frequency at f_3 , indicated by the black curve in Fig. 3a.

Figure 4a shows the electron η_3^{jkl} (blue) and ion η_{i3}^{jkl} (red) oscillations for the same parameter values as in Fig. 3b but for the longer time period between 0 s and 0.0025 s. As seen in Fig. 4b, the power spectra of both η_3^{jkl} and η_{i3}^{jkl} have an approximately exponential slope. Figures 5 and 6, which are for the same time period, show that some of the pulse-type features in the time series have close to a Lorentzian shape. The examples in Figs. 5 and 6 give, for the fitted Lorentzian functions, the scaling frequencies $f_s \approx 9 \text{ kHz}$ (Fig. 5b), $f_s \approx 13 \text{ kHz}$ (Fig. 6b), and $f_s \approx 11 \text{ kHz}$ (Fig. 6c). As the obtained f_s values agree approximately with the slope of the spectrum, it is concluded that the power spectra in Figs. 4b, 5b, and 6d are determined by Lorentzian pulses due to chaotic dynamics and that the Lorentzian pulses have approximately the same

widths. In the discussed model, with the frequency matching conditions in Eq. (15), the spectrum of LH oscillations (ω_3) is upshifted to the UH mode according to $\omega_2 = \omega_0 + \omega_3$. The UH oscillations could then scatter off density irregularities of the filamentary density striations into electromagnetic emissions that can be detected as the BUM in the SEE spectrum on the ground. It is therefore concluded that the experimentally observed exponential high-frequency flank of the BUM emission (Fig. 1) is evidence of deterministic chaos in wave interactions along the lines of those shown in the present simulations.

The temporal evolution is chaotic for $E_0 = 0.1 \text{ V m}^{-1}$ (Figs. 3b, 4, 5, and 6) but not for $E_0 = 0.001 \text{ V m}^{-1}$ (Fig. 3a). This is evidence that a threshold must be exceeded for chaotic time dependence. Because of temporal modulations in the multi-cell drift trajectories associated with Φ_D , plasma may cross separatrices in the $\mathbf{E}_D \times \mathbf{B}_g$ drift. Deterministic chaos seems to set in when the drift is fast enough for plasma to drift sufficiently far to cross a separatrix to drift around an adjacent potential extremum before the potential changes sign every half wave period and the drift direction reverses.

Whereas some of the pulse-type features in the time series have an approximately Lorentzian form, most of them are asymmetric, and the later pulse flank is generally steeper than the earlier flank. This asymmetry may indicate nonlinear steepening of the pulses. A careful look reveals that this is also the case for the reasonably symmetric Lorentzian pulses in Figs. 5 to 7. It is interesting that the skewness of a Lorentzian pulse does not affect its power spectrum (Maggs and Morales, 2011; Garcia and Theodorsen, 2018), such that asymmetric Lorentzian pulses contribute to an exponential power spectrum. However, it is not clear whether some of the skewed pulses observed in the present simulations can actually be considered to be skewed Lorentzian forms. This requires further investigation.

Finally, the scaling frequency f_s in the present model depends on E_0 , A_{01} , and A_{02} . Figure 7 shows a case for $E_0 = 0.2 \text{ V m}^{-1}$, $A_{01} = A_{02} = 0.4 \text{ V}$, and other parameter values, as for Figs. 4 to 6. The obtained f_s values for the fitted Lorentzian functions are typically a few kilohertz higher than for $E_0 = 0.1 \text{ V m}^{-1}$ and $A_{01} = A_{02} = 0.2 \text{ V}$ (Figs. 5 and 6). With increasing E_0 , f_s increases. However, experiments on pump power stepping at the SURF facility suggest that the slope of the BUM high-frequency flank is independent of the pump power (Wagner et al., 1999, their Fig. 9). The maximum effective radiated power (ERP) was about 150 MW, and the BUM flank was observed to have similar slopes for the pump power levels of -6 , -3 , and 0 dB relative to the maximum ERP.

The present simulation results are not consistent with this experimental result. As seen from Fig. 7, for which f_s values for the fitted Lorentzian functions in Fig. 7b and c are a few kilohertz larger than in Figs. 5 and 6, f_s depends on E_0 , A_{01} , and A_{02} . At this stage, possible reasons for this discrepancy may only be speculated upon. In the present study, only a

single density depletion associated with a single small-scale striation is considered. In reality, many striations are excited simultaneously. Theories (Mjølhus, 1983; Gurevich et al., 1995; Hall and Leyser, 2003) and numerical computations (Eliasson and Leyser, 2015) show that striations are electromagnetically coupled to one another through the electromagnetic Z mode. It is brought into question whether, for sufficiently high pump powers, the nonlinear processes of oscillations localized inside a striation are nonlinearly saturated. Increasing the pump power may then only result in more striations to be excited. This could account for the higher BUM intensity at higher pump power but with f_{sl} that depends on the localized interactions independent of pump power. However, this requires modelling of the physics on a global scale, with many striations and with nonlinear saturation for the involved oscillation amplitudes, which is beyond the scope of the present study.

6 Conclusions

The prominent BUM feature in the spectrum of electromagnetic emissions stimulated by powerful HF radio waves in the ionosphere commonly has an exponential high-frequency flank for pump frequencies near a harmonic of the ionospheric electron gyro frequency. Exponential power spectra have been shown to be a characteristic of deterministic chaos. As the BUM has been interpreted in terms of parametric four-wave interactions involving the electromagnetic pump field and EB, UH, and non-resonant LH modes (Huang and Kuo, 1994), a simplified two-fluid model of parametrically excited LH oscillations has been derived and studied by means of numerical simulations. The LH oscillations were taken to be localized in a cylindrical density depletion in the plane perpendicular to a homogeneous and static geomagnetic field. As such, they form cylindrical modes characterized by the frequency, an azimuthal mode number and radial wave number. The localized LH modes are associated with multi-cell plasma drift patterns. For sufficiently strong driving fields, the time signal of the LH electron and ion density fluctuations at a fixed position in the simulation plane exhibit an approximately exponential power spectrum, thereby being evidence of deterministic chaos. The exponential spectrum is connected to pulse-type features of Lorentzian form in the time signal.

As the parameter values in the simulations are reasonable within the ionospheric experiments, it is proposed that the observed exponential flank of the BUM is the result of deterministic chaos in the LH dynamics. According to the model of parametric interaction for the BUM, the beating of the LH oscillations with the pump field shifts the LH spectrum to the UH mode at frequencies above the pump frequency, where they could be converted into electromagnetic emissions and be observed on the ground. In view of the generality of the physics of deterministic chaos, it may be that similar pro-

cesses can occur in other regions of space plasma, for example, in ionospheric single- or multi-cell convection that is topologically modulated by fluctuations in the geomagnetic field.

Code availability. The simulation code is not publicly available.

Data availability. The experimental results used in this paper have been published by Carozzi et al. (2002).

Competing interests. The author has declared that there are no competing interests.

Disclaimer. Publisher's note: Copernicus Publications remains neutral with regard to jurisdictional claims made in the text, published maps, institutional affiliations, or any other geographical representation in this paper. While Copernicus Publications makes every effort to include appropriate place names, the final responsibility lies with the authors.

Acknowledgements. The author gratefully acknowledges the referee Paul Bernhardt for his comments on the paper.

Financial support. The publication of this article was funded by the Swedish Research Council, Forte, Formas, and Vinnova.

Review statement. This paper was edited by Elias Roussos and reviewed by Paul Bernhardt and Savely Grach.

References

- Carozzi, T. D., Thidé, B., Grach, S. M., Leyser, T. B., Holz, M., Komrakov, G. P., Frolov, V. L., and Sergeev, E. N.: Stimulated electromagnetic emissions during pump frequency sweep through fourth electron cyclotron harmonic, *J. Geophys. Res.*, 107, 1253, <https://doi.org/10.1029/2001JA005082>, 2002.
- Eliasson, B. and Leyser, T. B.: Numerical study of upper hybrid to Z-mode leakage during electromagnetic pumping of groups of striations in the ionosphere, *Ann. Geophys.*, 33, 1019–1030, <https://doi.org/10.5194/angeo-33-1019-2015>, 2015.
- Frisch, U. and Morf, R.: Intermittency in nonlinear dynamics and singularities at complex times, *Phys. Rev. A*, 23, 2673–2705, <https://doi.org/10.1103/PhysRevA.23.2673>, 1981.
- Garcia, O. E. and Theodorsen, A.: Skewed Lorentzian pulses and exponential frequency power spectra, *Phys. Plasmas*, 25, 014503, <https://doi.org/10.1063/1.5004811>, 2018.
- Greenside, H., Ahlers, G., Hohenberg, P., and Walden, R.: A simple stochastic model for the onset of turbulence in Rayleigh-Bénard convection, *Physica D*, 5, 322–334, [https://doi.org/10.1016/0167-2789\(82\)90026-4](https://doi.org/10.1016/0167-2789(82)90026-4), 1982.
- Gurevich, A. V., Zybin, K. P., and Lukyanov, A. V.: Stationary state of isolated striations developed during ionospheric modification, *Phys. Lett. A*, 206, 247–259, 1995.
- Gurevich, A. V., Carlson, H., Lukyanov, A. V., and Zybin, K. P.: Parametric decay of upper hybrid plasma waves trapped inside density irregularities in the ionosphere, *Phys. Lett. A*, 231, 97–108, 1997.
- Hall, J. O. and Leyser, T. B.: Conversion of trapped upper hybrid oscillations and Z mode at a plasma density irregularity, *Phys. Plasmas*, 10, 2509–2518, 2003.
- Hornung, G., Nold, B., Maggs, J. E., Morales, G. J., Ramisch, M., and Stroth, U.: Observation of exponential spectra and Lorentzian pulses in the TJ-K stellarator, *Phys. Plasmas*, 18, 082303, <https://doi.org/10.1063/1.3622679>, 2011.
- Huang, J. and Kuo, S. P.: A theoretical model for the broad upshifted maximum in the stimulated electromagnetic emission spectrum, *J. Geophys. Res.*, 99, 19569–19576, 1994.
- Istomin, Y. N. and Leyser, T. B.: Parametric decay of an electromagnetic wave near electron cyclotron harmonics, *Phys. Plasmas*, 2, 2084–2097, <https://doi.org/10.1063/1.871295>, 1995.
- Istomin, Y. N. and Leyser, T. B.: Parametric interaction of self-localized upper hybrid states in quantized plasma density irregularities, *Phys. Plasmas*, 5, 921–931, <https://doi.org/10.1063/1.872661>, 1998.
- Istomin, Y. N. and Leyser, T. B.: Electron acceleration by cylindrical upper hybrid oscillations trapped in density irregularities in the ionosphere, *Phys. Plasmas*, 10, 2962–2970, <https://doi.org/10.1063/1.1578637>, 2003.
- Karplyuk, K., Kolesnichenko, Y., and Oraevsky, V.: Interaction of magnetohydrodynamic waves in a bounded plasma, *Nucl. Fusion*, 10, 3–11, <https://doi.org/10.1088/0029-5515/10/1/001>, 1970.
- Langtangen, H. P. and Linge, S.: *Finite Difference Computing with PDEs*, SpringerOpen, Cham, Switzerland, ISBN 978-3-319-55456-3 <https://doi.org/10.1007/978-3-319-55456-3>, 2017.
- Leyser, T. B.: Stimulated electromagnetic emissions by high-frequency electromagnetic pumping of the ionospheric plasma, *Space Sci. Rev.*, 98, 223–328, <https://doi.org/10.1023/A:1013875603938>, 2001.
- Leyser, T. B.: Deterministic Chaos in Ionospheric Plasma Pumped by Radio Waves, *Geophys. Res. Lett.*, 48, e2021GL093892, <https://doi.org/10.1029/2021GL093892>, 2021.
- Leyser, T. B., Thidé, B., Derblom, H., Hedberg, Å., Lundborg, B., Stubbe, P., and Kopka, H.: Stimulated electromagnetic emission near electron cyclotron harmonics in the ionosphere, *Phys. Rev. Lett.*, 63, 1145–1147, <https://doi.org/10.1103/PhysRevLett.63.1145>, 1989.
- Maggs, J. E. and Morales, G. J.: Generality of Deterministic Chaos, Exponential Spectra, and Lorentzian Pulses in Magnetically Confined Plasmas, *Phys. Rev. Lett.*, 107, 185003, <https://doi.org/10.1103/PhysRevLett.107.185003>, 2011.
- Maggs, J. E. and Morales, G. J.: Origin of Lorentzian pulses in deterministic chaos, *Phys. Rev. E*, 86, 015401(R), <https://doi.org/10.1103/PhysRevE.86.015401>, 2012.
- Mjølhus, E.: On reflexion and trapping of upper-hybrid waves, *J. Plasma Phys.*, 29, 195–215, 1983.
- Mjølhus, E.: Parametric instabilities of trapped upper-hybrid oscillations, *J. Plasma Phys.*, 58, 747–769, 1997.

- Pace, D. C., Shi, M., Maggs, J. E., Morales, G. J., and Carter, T. A.: Exponential frequency spectrum and Lorentzian pulses in magnetized plasmas, *Phys. Plasmas*, 15, 122304, <https://doi.org/10.1063/1.3023155>, 2008.
- Shi, M., Pace, D. C., Morales, G. J., Maggs, J. E., and Carter, T. A.: Structures generated in a temperature filament due to drift-wave convection, *Phys. Plasmas*, 16, 062306, <https://doi.org/10.1063/1.3147863>, 2009.
- Wagner, L. S., Bernhardt, P. A., Goldstein, J. A., Selcher, C. A., Frolov, V. L., and Sergeev, E. N.: Effect of ionospheric self-conditioning and preconditioning on the broad upshifted maximum component of stimulated electromagnetic emission, *J. Geophys. Res.*, 104, 2573–2590, <https://doi.org/10.1029/1998JA900006>, 1999.
- Xi, H. and Scales, W. A.: Numerical simulation studies on the broad upshifted maximum of ionospheric stimulated electromagnetic emission, *J. Geophys. Res.*, 106, 12787–12801, 2001.